PAUL SCHERRER INSTITUT

SWISS LIGHT SOURCE SLS

SLS-TME-TA-2010-0320
10th March 2010

Halo background in laser beam slicing experiments at SLS and SOLEIL

Andreas Streun

Paul Scherrer Institut, CH-5232 Villigen PSI, Switzerland

Most of the background noise in a laser beam slicing experiment for generation of sub-ps X-ray pulses is due to a beam halo formed from the relics of previous laser beam interactions. Thus the signal to noise ratio deteriorates if the laser repetition frequency is increased. In the context of a planned laser beam slicing installation at SOLEIL for the CRISTAL and TEMPO beam lines, and a planned upgrade of the existing SLS installation for the μXAS/FEMTO beam line, we will investigate the signal to noise ratio as a function of the laser repetition rate and compare it to tracking simulations and to measurements done at SLS FEMTO.

Contents

1 Introduction

In a laser beam slicing setup for generation of sub-ps X-ray pulses, a laser beam modulates the energy of electrons in a wiggler (the modulator). Dispersive elements following the modulator translate the energy modulation into a horizontal separation. In a subsquent undulator (the radiator), the modulated electrons emit synchrotron radiation at an angular and/or spatial offset. Slits located in the beam line suppress the core beam radiation and transmit only radiation from electron with energies above some threshold level in order to extract sub-ps X-ray pulses.

The modulated electrons are not lost from the beam but stay well inside the machine acceptance, thus they will perform betatron and synchrotron oscillations (very similar to Touschek scattered particles). Decoherence due to linear and non-linear amplitude and energy dependancy of the betatron oscillations leads to fast filamentation and forms an isotropic beam halo within a few 100 turns. Eventually the beam halo merges back into the core beam due to radiation damping.

Since the laser repetition time (< 1 ms) is shorter than the radiation damping times of the storage ring (several ms), the halo is fed with new particles while others merge back to the core. Thus an equilibrium beam halo will form which is composed from the relics from a number of previous laser beam interactions. Obviously, the population of the halo increases with the laser repetition rate.

Radiation from the halo electrons will be transmitted partially by the apertures of the beam line and provide a background to the experiment. Thus, the apertures of the beam line have to be set for maximum signal and minimum halo transmission. This is best achieved by a pair of slits orthogonal in phase space in order to fit the acceptance to the signal's phase space area. Orthogonality requires a focusing element in the beam line which is usually realized by a toroidal mirror providing horizontal and vertical focussing for point-to-point imaging from the [virtual] source point to the experiment.

In this paper we will calculate the signal and halo intensitities for this kind of set up and develope a strategy how to optimize the ratio of both. An analytical model will be established and compared to simulations and measurements at SLS-FEMTO. This paper is a continuation and further elaboration of previous work on the subject [14, 8, 15].

2 Laser beam slicing layouts

Fig. 1 shows the schemes of laser beam slicing as already in use at SLS-FEMTO [16] and as proposed for SOLEIL [10]. At SLS, a dedicted magnet chicane had been installed to translate the energy modulation to horizontal separation, whereas at SOLEIL the storage ring arc performs this task. At BESSY-II (not shown) a dipole was installed between modulator and radiator located in the same straight [2]. Radiation emitted from electrons that received an energy modulation is extracted by a system

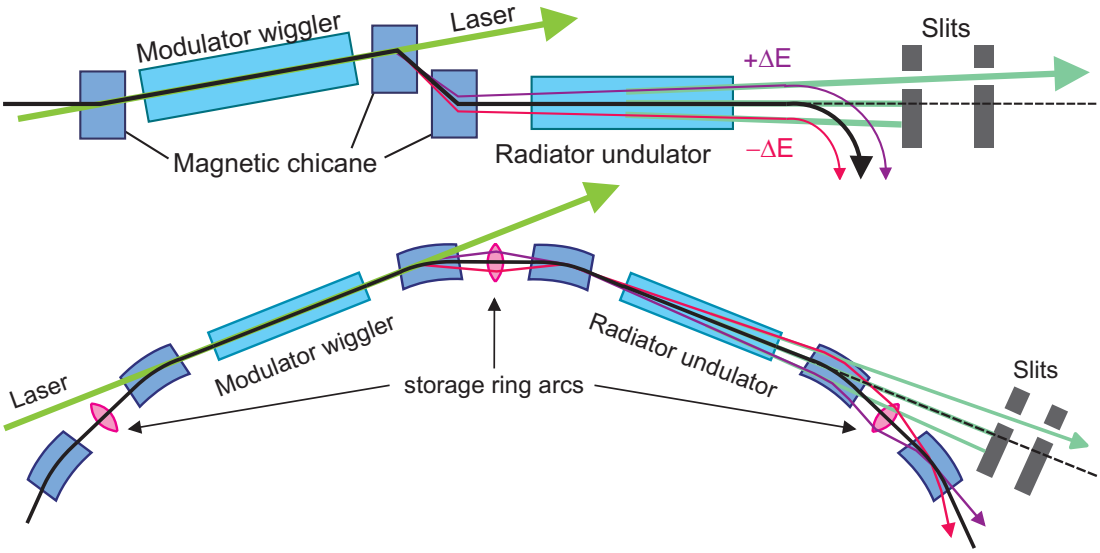

Figure 1: Schematic layout of the existing SLS-FEMTO installation (top) and of the proposed laser slicing installation at SOLEIL (bottom)

of apertures (front end slits), whereas the radiation from the beam core and from the dipoles between modulator and radiator is blocked.

The basic layout of a beam line for point to point imaging of the [virtual] source to the experiment is shown in fig. 2: relevant elements for our purpose are the front end (FE) and beam line (BL) slits, and the focusing element (toroidal mirror) between. We only consider the horizontal plane, where the separation is done.

The basic layout as shown in fig 2 corresponds to the μXAS/FEMTO beam line at SLS [9] and to the two beamlines CRISTAL and TEMPO at SOLEIL which are foreseen to make use of the sub-ps X-ray pulses. The corresponding radiator undulators are located one, resp. four arcs downstream the modulator wiggler. Storage ring parameters for SLS and SOLEIL, and beam line parameters are given in appendix A.

3 Beam dynamics

3.1 Modulated beam dispersion

An electron beam in a storage ring has a Gaussian distribution in the 6 dimensions $x, x', y, y', s, \delta = \Delta E/E$. The modulation due to laser interaction leads to a non-Gaussian δ-distribution in a rather thin (in s) slice of the bunch. So we call δ the energy a particle has due to the Gaussian distribution, and $\tilde{\delta}$ the energy from the laser modulation. Thus, the 2-d horizontal transformation of a particle from the modulator (index m) to the radiator (index r) is given by

$$\vec{x}_r = \vec{\eta}_r(\delta + \tilde{\delta}) + M_{rm}(\vec{x}_m - \vec{\eta}_m(\delta + \tilde{\delta})) \quad (1)$$

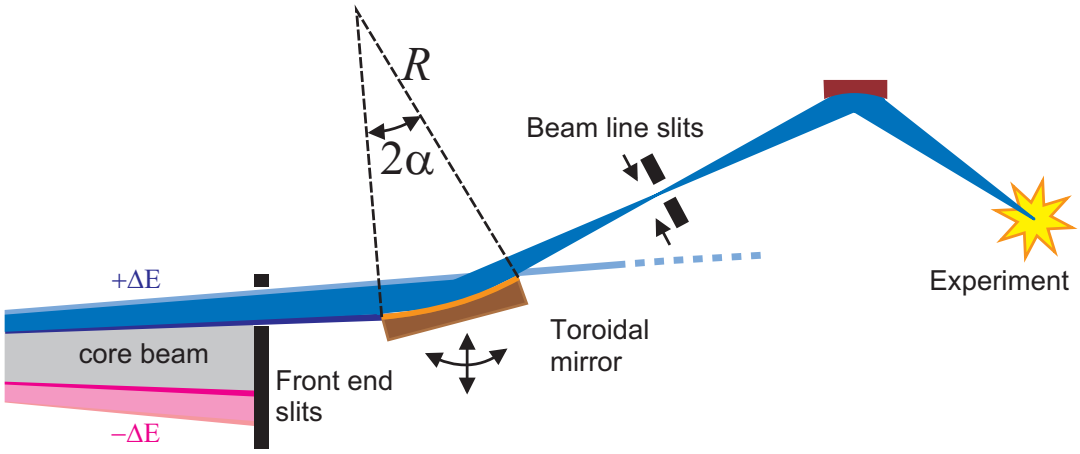

Figure 2: Schematic layout of a beamline using photons from laser beam interaction.

$\vec{\eta}$ are the local dispersion vectors and M_{mr} is the 2×2 horizontal matrix for transfer from "m" to "r" given by

$$M_{mr} = T_r^{-1}\, R(\Delta\mu_{rm})\, T_m \;\text{ with } T = \begin{pmatrix} \frac{1}{\sqrt{\beta}} & 0 \\ \frac{\alpha}{\sqrt{\beta}} & \sqrt{\beta} \end{pmatrix}, \quad R(\phi) = \begin{pmatrix} \cos\phi & \sin\phi \\ -\sin\phi & \cos\phi \end{pmatrix} \tag{2}$$

R is a rotation matrix[1], $\Delta\mu_{rm}$ the horizontal betatron phase advance between the two points, and T the transformation of the local beam ellipse to a circle of radius $\sqrt{\epsilon}$, with α, β, γ the Twiss parameters and ϵ the emittance.

Eq.1 expresses the fact, that the dispersive orbit is the center of motion for the betatron oscillation. Extracting only the modulation contribution $\tilde{\delta}$ by assuming an ideal closed orbit particle ($x_m = 0$, $x'_m = 0$, $\delta = 0$) in eq.1 and dividing by $\tilde{\delta}$ we get the propagation of dispersion for the modulated electrons[2]:

$$\tilde{\vec{\eta}}_r = \vec{\eta}_r - M_{rm}\vec{\eta}_m \tag{3}$$

The same dispersion is obtained from a lattice code by starting the beam at the modulator and setting $\tilde{\vec{\eta}}_m = 0$.

3.2 Normalized phase space

The equation of a modulated particle from the beam core in normalized phase space (χ, χ') at the location of the radiator is obtained by multiplication with T_r:

$$\vec{\chi}_r = T_r\vec{x} = T_r\vec{\eta}_r\tilde{\delta} - R(\Delta\mu_{rm})T_m\vec{\eta}_m\tilde{\delta} \tag{4}$$

[1]Note, that the matrix R corresponds to a counter-clockwise, i.e. mathematically positive rotation for $\phi > 0$, however bounded motion in (x, x') phase space corresponds to a clockwise rotation, i.e. the betatron phase is a negative number.

[2]Eq.3 is equivalent to eq.(1) in [10]

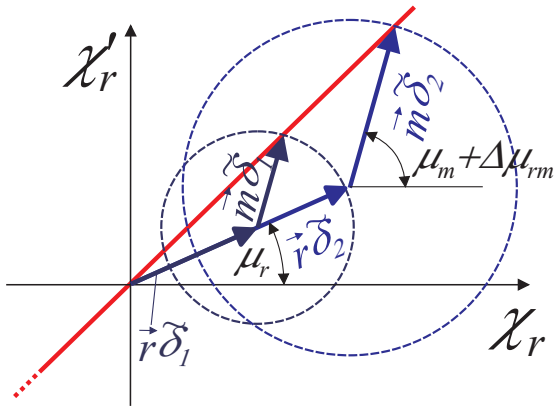

Figure 3: Schematic view of phase space distribution

In normalized horizontal phase space (χ, χ') the modulated electrons are initially aligned along the red line, which is composed from the dispersion in the radiator ($\vec{r}$) and the betatron amplitude excited by the change of energy in the modulator ($\vec{m}$).

Since in normalized phase space the betatron motion is bound to a circle, it is convenient to introduce amplitude and angle of the dispersion function:

$$\mathcal{H} = (T\vec{\eta})^2 = \gamma\eta^2 + 2\alpha\eta\eta' + \beta\eta'^2 \qquad \mu = \arctan\left(\frac{\alpha\eta + \beta\eta'}{\eta}\right) \tag{5}$$

Then the particle coordinate is given by

$$\vec{\chi}_r = \underbrace{\sqrt{\mathcal{H}_r}\begin{matrix}\cos\\ \sin\end{matrix}(\mu_r)\,\tilde{\delta}}_{:=\vec{r}} - \underbrace{\sqrt{\mathcal{H}_m}\begin{matrix}\cos\\ \sin\end{matrix}(\Delta\mu_{rm}+\mu_m)\,\tilde{\delta}}_{:=-\vec{m}} \tag{6}$$

If both radiator and modulator are located near symmetry points, where $\alpha \approx \eta' \approx 0$, it is obvious, that a phase advance $\Delta\mu_{rm} = \pi$ provides optimum spatial separation. The situation for two values of $\tilde{\delta}$ is shown in fig.3: the modulated particles are aligned along the red line.

Eq.6 and fig.3 show two contributions to separation: the first term, $\vec{r}\tilde{\delta}$, is the orbit due to the local dispersion of the radiator, the second term, $\vec{m}\tilde{\delta}$, is related to the betatron amplitude the particle received due to local dispersion when its energy was changed in the modulator. The evolution in time is different for the two contributions: The modulation energy will oscillate slowly with the synchrotron tune ν_s and damp exponentially with the longitudinal damping time τ_s, asymptotically approaching the natural energy spread σ_δ. The betatron amplitude will oscillate fast with the betatron tune ν_x and damp exponentially with the horizontal damping time τ_x, asymptotically reaching the natural horizontal emittance ϵ. So, for turn n, resp. time $t = nT_o$, with T_o the revolution time, eq.6 becomes

$$\vec{\chi}_{rn} = \left(e^{-nT_o/\tau_s}\cos(2\pi n\nu_s)\,\vec{r} + e^{-nT_o/\tau_x}R(2\pi n\nu_x)\,\vec{m}\right)\,\tilde{\delta}_o \tag{7}$$

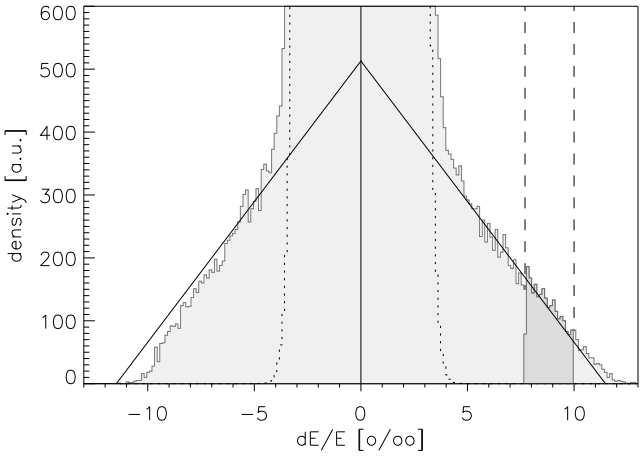

Figure 4: Particle distribution as a function of energy.
The core beam distribution alone (before laser modulation) is shown as dotted line. The front end (FE) slits define an interval of electron energy (dashed lines) from which the emitted photons are accepted. The distribution is well approximated by a linear function (triangle). However note the slight asymmetry of the distribution due to the "Guoy phase shift" effect. The histogram is based on simulation data [3] for 3 mJ laser pulse energy.

Here $\tilde{\delta}_o$ is the initial, individual energy modulation of the particle. Since we are only interested in high amplitudes, i.e. amplitudes large compared to natural emittance and energy spread, the asymptotic values of the damping functions have been neglected.

3.3 Distribution of energy modulations

In order to establish a simple analytical model, and since we are not interested in the core beam region, we may well approximate the energy distribution of the modulated electrons by a linear density function as shown in fig. 4 (normalized to unity):

$$\rho(\tilde{\delta}) = \frac{dN}{d\tilde{\delta}} = \frac{1}{\tilde{\delta}_p}\left(1 - \frac{|\tilde{\delta}|}{\tilde{\delta}_p}\right), \qquad |\tilde{\delta}| \leq \tilde{\delta}_p \tag{8}$$

With $\tilde{\delta}_p$ the maximum (peak) value of $\tilde{\delta}$ received in modulation. This distribution is valid at any time t, since all energies will follow the same temporal evolution, which has been explicitly introduced already in eq.7. So we only need to consider the distribution of initial energies.

Eq.8 is a 1-dimensional distribution and leads to a normalized phase space distribution shown as the red line in fig.3 for "turn 0", i.e. immediately after modulation. Later, each particle performs a fast betatron oscillation following a circle with midpoint and radius given by its individual energy $\tilde{\delta}$. The midpoint vector oscillates slowly with the

synchrotron tune. The betatron oscillation will show rather fast filamentation due to decoherence and nonlinearities, so for estimates of halo intensities we may simplify the model by assuming isotropically populated circles for each value $\tilde{\delta}_o$, weighted by eq.8. In sec. 4 and 5 we will integrate the resulting particle distribution over the phase space acceptance area defined by the FE and BL apertures by calculating the visible arcs of these circles.

3.4 Effective photon emittance

The size of the photon beam depends on the beam line optics and on the photon emittance. Dispersion and diffraction lead to an effective photon beam emittance which is larger than the electron emittance. This may become relevant when filtering the photon beam at the slits in order to extract the signal and suppress core and halo beam.

In case of non-zero stored beam dispersion $\vec{\eta}_r$ in the radiator (as it is the case for SOLEIL), effective emittance and Twiss parameters are obtained from a convolution of the 2-d distribution in (x, x') with the 1-d distribution in δ:

$$\epsilon_{\text{eff}} = \sqrt{\epsilon^2 + \epsilon \mathcal{H}_r \sigma_\delta^2}\,, \qquad \beta_{\text{eff}} = \frac{\epsilon\beta_r + (\eta_r \sigma_\delta)^2}{\epsilon_{\text{eff}}}\,, \qquad \alpha_{\text{eff}} = \frac{\epsilon\alpha_r - \eta\eta_r' \sigma_\delta^2}{\epsilon_{\text{eff}}}. \tag{9}$$

with $\mathcal{H}$ the dispersion's amplitude (also called lattice invariant) from eq.5 and σ_δ the natural energy spread.

Diffraction creates a finite photon beam phase space which has to be convoluted with the effective electron beam phase space. Emittance and beta function describing the diffraction phase space of a single photon at wavelength λ, emitted from an undulator of length L are appoximately given by [6]

$$\epsilon_d \approx \frac{\lambda}{4\pi} \qquad \beta_d \approx \frac{L}{4\pi} \qquad \alpha_d \approx 0 \tag{10}$$

The convolution with the electrons' phase space is given by [6, 13]

$$\epsilon_{\text{phot}}^2 = \epsilon^2 + \epsilon_d^2 + \epsilon\,\epsilon_d \left(\frac{\beta}{\beta_d} + \gamma\beta_d\right) \quad \beta_{\text{phot}} = \frac{\epsilon\beta + \epsilon_d\beta_d}{\epsilon_{\text{phot}}} \quad \alpha_{\text{phot}} = \frac{\epsilon\alpha}{\epsilon_{\text{phot}}} \tag{11}$$

Using photons in the keV-range, resp. wavelengths $\lambda < 10$Å, we usually neglect diffraction since $\epsilon > 1$ nm $\gg \epsilon_d \approx 0.1$ nm, i.e. the horizontal photon phase space is assumed to be identical to the electron phase space[3]. This approximation is well fulfilled for SLS-FEMTO and SOLEIL-CRISTAL but not for SOLEIL-TEMPO at low photon energy (100 eV). Even in cases where $\epsilon \gg \epsilon_d$, the mismatch of diffraction and electron phase spaces may lead to an emittance increase of the photon beam, because β is much larger than β_d ($\approx 0.1 \ldots 0.2$ m), in particular for SOLEIL.

[3]Vertically this is not at all the case, however since we investigate horizontal separations schemes, we don't need to consider that.

3.5 The virtual source point

Seen from the beam line, the beam is emitted from a virtual source point at a distance L_v upstream, which is (neglecting diffraction) given by

$$L_v = -\frac{\alpha_{\text{eff}}}{\gamma_{\text{eff}}} = -\frac{\epsilon\alpha - \eta\eta'\sigma_\delta^2}{\epsilon\gamma + \eta'^2\sigma_\delta^2} \tag{12}$$

The effective Twiss parameters at the virtual source are thus given by

$$\beta_{v,\text{eff}} = \beta_{\text{eff}} - \frac{\alpha_{\text{eff}}^2}{\gamma_{\text{eff}}} \qquad \alpha_{v,\text{eff}} = 0 \qquad \gamma_{v,\text{eff}} = \gamma_{\text{eff}} \tag{13}$$

For the extreme cases of an emittance dominated beam with a 2-dimensional distribution, where the source is of finite size, and of a dispersion dominated beam, with a 1-dimensional distribution, where the source is a point, we obtain the limits

$$\vec{\eta} \longrightarrow \vec{0}: \quad L_v \longrightarrow L_{v\epsilon} = -\frac{\alpha}{\gamma} \qquad \epsilon \longrightarrow 0: \quad L_v \longrightarrow L_{v\eta} = \frac{\eta}{\eta'} \tag{14}$$

For the laser modulated beam, we have to use the modulated dispersion $\tilde{\vec{\eta}}$ from eq.3. The virtual source distances $L_{v\tilde{\eta}}$ and $L_{v\epsilon}$ thus may be different, limiting the minimum achievable beam size at a focus in the beamline.

3.6 Slicing efficiency

The analytical model has to be calibrated in order to compare it to particle tracking and experiments.

The simulation of laser beam interaction leading to fig. 4 was done tracking N_s particles uniformely distributed in a time interval ΔT. The fraction of particles contained in the triangular area $N_\triangle$ is obtained by

$$N_\triangle = N_s \cdot F_\triangle \qquad F_\triangle = \frac{\text{triangle area}}{\Sigma \text{ histogram}} \tag{15}$$

The fraction of charge, or number of electrons in the slice, compared to the total charge of the Gaussian distributed electron bunch of rms length σ_t is given by the factor

$$F_s = \frac{\text{slice charge}}{\text{bunch charge}} = \frac{\Delta T}{\sqrt{2\pi}\sigma_t} \tag{16}$$

So, the intensity of the signal S transmitted by front end and beam line has to be multiplied with these factors to obtain the *buch slicing efficieny* SE:

$$\text{SE} = F_\triangle \cdot F_s \cdot S \tag{17}$$

The bunch slicing efficiency thus gives the fraction of sliced beam to core beam intensity. This assumes gating of the experiment on the time scale of the bunch repetition

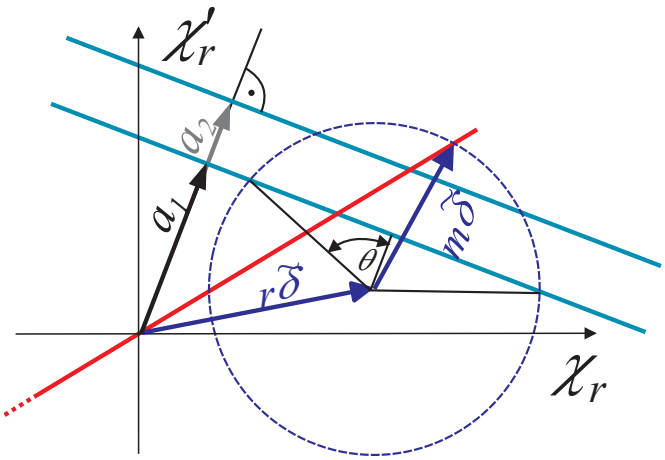

Figure 5: Phase space corridor formed by the FE slits

rate, i.e. no light from other, unsliced bunches can be seen. *Total slicing efficiency* is the ratio of total flux for the laser slicing experiment to the total flux for the other users. With I_o total current, and I_s the current of the single bunch used for slicing, T_o the revolution time of the storage ring, and f_L the slicing rep.rate, the total slicing efficiency thus is

$$\mathrm{SE}_{\mathrm{total}} = \mathrm{SE} \cdot T_o f_L \frac{I_s}{I_o} \tag{18}$$

Of course, in eq.16 the length of the sliced bunch has to be used, which may be lengthened due to its larger current. Details of the beam line, e.g. reflectivity of monochromators, reduce normal and sliced beam flux in the same way and thus do not affect the slicing efficieny.

The core beam background C is obtained from integration of the [Gaussian] core distribution over the FE and BL apertures, and weighted by $1/(F_{\triangle} F_s)$, to normalize it to the signal S and halo H results.

4 Front end (FE) acceptance

The FE slits suppress the core beam and dipole radiation. Since the modulated electrons are "sorted" horizontally due to dispersion, the FE-slits also select the energy acceptance of the beam line. However, the acceptance may already be limited due to the finite length of the toroid, as it is the case for SLS-FEMTO and sketched in fig.2. In this case, the movable FE slits are adjusted to meet these limits in order to protect the toroid.

The inner and outer blade of the FE slits located at a distance L_f from the reference point, i.e. the radiator centre, may be at horizontal positions $x_{1,2}$ (also see fig.6 below). Backtransformation to the reference point and transformation to normalized

phase space, using eq.2,

$$\vec{\chi} = T_r \cdot \begin{pmatrix} 1 & -L_f \\ 0 & 1 \end{pmatrix} \cdot \begin{pmatrix} x_{1,2} \\ \lambda \end{pmatrix} \qquad \lambda \in \boldsymbol{R}, \tag{19}$$

defines the corridor of FE acceptance shown in fig5:

$$\vec{\chi} = \vec{\chi_{1,2}} + \vec{d}\lambda \quad \text{with} \quad \vec{\chi}_{1,2} = \begin{pmatrix} 1/\sqrt{\beta_r} \\ \alpha_r/\sqrt{\beta_r} \end{pmatrix} \cdot x_{1,2}, \quad \vec{d} = \begin{pmatrix} -L_f/\sqrt{\beta_r} \\ \sqrt{\beta_r} - \alpha_r L_f/\sqrt{\beta_r} \end{pmatrix},$$

The vector of minimum distance of the slit blades to the origin is given by

$$\vec{a}_{1,2} = \vec{\chi}_{1,2} - \frac{(\vec{\chi}_{1,2} \cdot \vec{d})\,\vec{d}}{d^2} \tag{20}$$

4.1 FE signal acceptance

The modulated beam photons, which (neglecting emittance) are aligned along the dispersion vector, are shown as red line in fig.5. The interval of "visible" energies is given by geometry:

$$\tilde{\delta}_{1,2} = \min\left(\frac{a_{1,2}^2}{\vec{a}_{1,2} \cdot (\vec{r} + \vec{m})}\,;\, \tilde{\delta}_p\right) \tag{21}$$

Of course, $\tilde{\delta}_p$, the peak modulation is the limit. Integration of eq.8 gives the turn-0 signal transmitted by the FE slits:

$$S^{\mathrm{FE}} = \int_{\tilde{\delta}_1}^{\tilde{\delta}_2} \rho(\tilde{\delta})\, d\tilde{\delta} = \frac{\tilde{\delta}_2 - \tilde{\delta}_1}{\tilde{\delta}_p} - \frac{\tilde{\delta}_2^2 - \tilde{\delta}_1^2}{2\tilde{\delta}_p^2} \tag{22}$$

For finite emittance, the integral from eq.22 has to be modified for including the Gaussian beam profile: We introduce a unit vector $\hat{\vec{a}}$ pointing in direction of the vectors $\vec{a}_{1,2}$ and integrate along this direction:

$$S^{\mathrm{FE}} = \frac{1}{\sqrt{2\pi\,\epsilon}\,\tilde{\delta}_p} \int_{-\tilde{\delta}_p}^{+\tilde{\delta}_p} \int_{a_1}^{a_2} \exp\left(-\frac{(u - \hat{\vec{a}} \cdot (\vec{r} + \vec{m})\,\tilde{\delta})^2}{2\epsilon}\right) \left(1 - \frac{|\tilde{\delta}|}{\tilde{\delta}_p}\right) du\, d\tilde{\delta}$$

Here, to each energy $\tilde{\delta}$ belongs a Gaussian distribution displaced by dispersion. The solution agrees within 2% for beam emittances up to 200 nm with eq.22 for typical parameters of SLS-FEMTO, therefore neglecting the emittance seems to be well justified.

4.2 FE halo acceptance

The halo intensity H is given by integrating the photon distribution over the area of the FE-corridor in fig. 5. Each energy has to be weighted with the visible arc ratio and with the density function from eq.8:

$$H^{\mathrm{FE}} = \int_{-\tilde{\delta}_p}^{+\tilde{\delta}_p} \frac{2\theta_2(\tilde{\delta}) - 2\theta_1(\tilde{\delta})}{2\pi}\, \rho(\tilde{\delta})\, d\tilde{\delta} \tag{23}$$

where the angle is given by geometry (see fig.5):

$$\theta_{1,2} = \arccos\left(\frac{a_{1,2}}{m}\cdot\frac{1}{\tilde{\delta}} - \frac{\vec{a}_{1,2}\cdot\vec{r}}{a_{1,2}\,m}\right) \tag{24}$$

For the case of SLS-FEMTO with no dispersion in the radiator, i.e. $\vec{r}=0$, an elegant analytical solution was found [15]. An analytical solution exists for the general case too, but it is not "nice" and complicated by several case distinctions depending on sign and magnitude of $\tilde{\delta}$. Therefore, a semi-analytical, less elegant method was chosen which proceeds simply by calculating the visible arc angle for a table of $\tilde{\delta}$-values and summation, but still executes much faster than particle tracking.

4.3 FE core beam acceptance

The transmitted core beam is simply given by integration of the Gaussian distribution over the corridor defined by the FE-slits:

$$C^{\mathrm{FE}} = \frac{1}{2}\left(\mathrm{erfc}\left(\frac{a_1}{\sqrt{2\epsilon}}\right) - \mathrm{erfc}\left(\frac{a_2}{\sqrt{2\epsilon}}\right)\right)\frac{1}{F_\triangle\,F_s} \tag{25}$$

The factor $1/2$ takes into account, that core beam is transmitted only to one side. The factors from eqs.15,16 take into account that the core signal comes from the whole bunch, not only from the slice.

5 Beam line (BL) acceptance

If the toroid of the beamline as sketched in fig.2 is adjusted to create a focus at the BL slits, an efficient suppression of the halo can be achieved by closing the slits while little affecting the signal.

The transfer matrix for imaging from the virtual source ("v") of the beam to the BL slits ("b") is given by

$$M_{vb} = \begin{pmatrix} 1 & L_b \\ 1 & 1 \end{pmatrix}\cdot\begin{pmatrix} -1 & 0 \\ F & -1 \end{pmatrix}\cdot\begin{pmatrix} 1 & L_v \\ 0 & 1 \end{pmatrix}, \tag{26}$$

with L_v the distance from the source to the toroid, see eq.12, and L_b the distance from toroid to BL-slits. $F = 1/f = 2/(R\sin\alpha)$ is the horizontal toroid focusing strength from eq.43 in appendix B, with R the tangential radius and α the incident angle. Assuming the distances are given, the solution for F is obtained from

$$\vec{x}_b = M_{vb}\cdot\vec{x}_v \quad \text{and} \quad M_{vb} \stackrel{!}{=} \begin{pmatrix} \mathcal{M} & 0 \\ \dots & \mathcal{M}^{-1} \end{pmatrix} \tag{27}$$

with the result $F = 1/f = 1/L_v + 1/L_b$ for a point-to-point image with magnification $\mathcal{M} = L_b/L_v$.

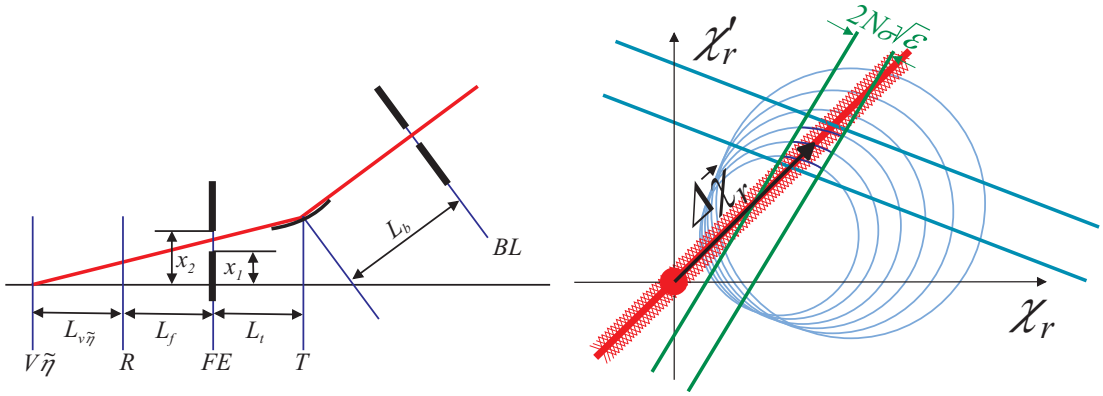

Figure 6: FE and BL slits in phase space

The stored beam is represented by the solid red circle of radius $\sqrt{\epsilon}$ at the origin. The modulation forms a line of same thickness in normalized phase space. FE and BL slits appear as cyan and green corridors. The left figure explains the coordinate offset $\Delta\vec{\chi}_r$ for backtransformation of BL slits.

This solution is only approximately correct for finite emittance. The exact solution is obtained from

$$0 \stackrel{!}{=} \alpha_b = -m_{11}m_{21}\beta_v - m_{12}m_{22}\frac{1}{\beta_v}$$

since $\alpha_v = 0$ at the virtual source, see eq.13. Using the matrix from eq.26 and solving for F gives the exact solution. However, for small emittance the result is close to the approximate solution (for SLS-FEMTO the difference is 0.5%).

The backtransformation of the BL-slits to the reference point (radiator) is similar to the FE-slits backtransformation from eq.19, but instead of a negative drift we have the inverse of the transfer matrix from the radiator to the BL-slit M_{rb}, and an offset $\Delta\vec{\chi}_r$, because the beam line coordinate system has a spatial and angular shift compared to the reference system, which is determined by the central ray passing the FE-slits. From fig.6 can be seen, that

$$\Delta\vec{\chi}_r = T_r \begin{pmatrix} L_{v\tilde{\eta}} \\ 1 \end{pmatrix} \cdot \frac{x_1 + x_2}{2(L_{v\tilde{\eta}} + L_f)}$$

Correspondingly, $(\vec{r} + \vec{m})\tilde{\delta} = \Delta\vec{\chi}_r$ defines the central modulation energy accepted. The backtransformation of the BL-slits as sketched in fig.6 is then given by

$$\vec{\chi} = R(-\Delta\mu_{rb})T_b \begin{pmatrix} \pm x_b \\ \kappa \end{pmatrix} + \Delta\vec{\chi}_r \qquad \kappa \in \boldsymbol{R} \tag{28}$$

5.1 BL signal acceptance

Closing the beam line slits to $\pm N_\sigma$ rms beam radii thus scratching off the tails of the Gaussian attenuates the signal from eq.22 by a factor

$$2\int_0^{N_\sigma} \frac{e^{-u^2/2}}{\sqrt{2\pi}} du \quad \Longrightarrow \quad S^{\rm BL} = \mathrm{erf}\left(\frac{N_\sigma}{\sqrt{2}}\right) \cdot S^{\rm FE} \tag{29}$$

where $N_\sigma = x_b/\sigma_b$ and $\sigma_b = \sqrt{\beta_b \epsilon}$ with β_b obtained from application of either M_{rb} or M_{vb} from eq.26 to the effective source parametersfrom eq.13. Alternatively we may just use the beam line magnification: $\sigma_b = \mathcal{M}\sigma_v$.

This is only correct if the angle of inclination between the BL-slits in phase space and the signal distribution (green and red lines in fig.6) is not too large. Otherwise near the FE-blades the cut of the Gaussian will become asymmetric and lead to a reduced signal.

5.2 BL halo acceptance

The procedure is similar like for the FE-slits and straightforward though a bit tedious: the halo intensity is obtained from the integral resp. sum over the particle distribution "visible" inside the rhomboid area ($\diamond$) area formed by the intersection of the FE and BL corridors as shown in fig.6, schematically written as

$$H^{\rm BL} = \int_{-\tilde{\delta}_p}^{+\tilde{\delta}_p} \frac{\theta_\diamond(\tilde{\delta})}{2\pi}\, \rho(\tilde{\delta})\, d\tilde{\delta} \tag{30}$$

Practically, we determine the visible arc length of each circle as a function of $\tilde{\delta}$, multiply by the density function and summarize. The rhomboid corner vectors are obtained from elimination of λ and κ in eqs.19,28.

5.3 BL core beam acceptance

The core beam accepted by the rhomboid is approximately and most easily obtained from the average density, i.e. averaging the values of the Gaussian distribution at the rhomboid corners $\{\vec{\chi}\}_k$ (in cyclic order!) multiplied with the rhomboid area:

$$C^{\rm BL} \approx \frac{1}{4}\sum_{k=1}^{4} e^{-\vec{\chi}_k^2/(2\epsilon)} \cdot \frac{1}{2}\left|\sum_{k=1}^{4} \vec{\chi}_k \times \vec{\chi}_{k+1-4[k/4]}\right| \frac{1}{F_\triangle\, F_s} \tag{31}$$

6 Repetition rate

Since the time between laser beam interactions is much shorter than the radiation damping time, the total halo signal is composed from many halos left over from previous interactions. Due to radiation damping the halo shrinks and finally approaches the equilibrium beam parameters of the core beam. As long as the amplitude is large

compared to the beam emittance and natural energy spread the linear distribution will be maintained, because the dynamics far above equilibrium is dominated by classical damping. So for any time t or turn number $n = t/T_o$ after the laser slicing the halo calculations above are still valid, if we just replace the circle midpoint vectors and their radii by the time dependant values (see eq.7):

$$\vec{r} \;\longrightarrow\; \vec{r}_n = \vec{r} \cdot e^{-nT_o/\tau_s} \cos(2\pi n \nu_s) \qquad m \;\longrightarrow\; m_n = m \cdot e^{-nT_o/\tau_x}$$

The laser repetition time has to be an integer multiple p of the turn number: $T_{\mathrm{rep}} = pT_o$. Then the total halo intensity is composed from all halos retarded by multiples of p turns:

$$H_{\mathrm{total}}^{\mathrm{FE/BL}} = \sum_{k=1}^{K} H_{k \cdot p}^{\mathrm{FE/BL}} \tag{32}$$

The upper limit of summation K is reached when the amplitude corresponding to the peak energy modulation disappears behind the inner blade of the FE-slit, see fig.5:

$$\left(\frac{\vec{a}_1 \cdot \vec{r}}{a_1} \cdot e^{-KT_o/\tau_s} + m \cdot e^{-KT_o/\tau_x} \right) \tilde{\delta}_p = a_1 \quad \longrightarrow \quad K$$

Here, the synchrotron osciallation term at $\vec{r}$ was dropped, because only shrinking due to damping guarantees that the halo does not come back again. At an earlier turn $< K$, the halo transmitted by the FE/BL intersection rhomboid may disappear already.

7 Particle tracking

The storage ring lattices for SLS and SOLEIL with parameters given in appendix A were tracked using the program TRACY-2 [5]. The equilibrium beam parameters and local Twiss parameters at the modulator centre were entered into an IDL-program for laser beam simulation[4]. The program established a 6-dimensional ensemble of particles representing a thin slice in the center of the electron bunch: The longitudinal coordinate $\Delta s/c$ has a uniform distribution over an interval of ± 106 fs, corresponding to $\pm 5\sigma$ of a laser pulse with 50 fs FWHM in power, and the other dimensions have Gaussian distributions with the stored beam parameters.

The modulation was calculated by integration of the particle motion through the modulator wiggler and the superimposed electric field of the laser. For simplicity, the parameters of SLS/FEMTO were used for all runs and scaled to the SOLEIL case, since details of the modulation process (wiggler field, laser wavelength, laser pulse length etc.) are not relevant for the calculation of signal to halo ratio and its evolution: this depends only on the modulation amplitude, the electron beam parameters, the radiation damping time and the beamline geometry.

The modulated particle ensemble's coordinates were then transferred to TRACY-2. In order to save computing time, particles with total energy $|\tilde{\delta} + \delta| < \delta_{\mathrm{cut}}$ were

[4]Program written by Paul Beaud, PSI, with minor modifications by the author.

ignored, where δ_{cut} was chosen at least 3 standard deviations of the natural energy spread, because they must never enter the beam line – otherwise the core beam tails could enter too and would spoil the experiment anyway. This reduced the $N_o = 100000$ particles used for the laser beam simulation to about 30000 for tracking. Table 1 shows parameters from laser beam interaction simulations which were used for the analytical treatment.

Table 1: Parameters from laser beam interaction simulations (2.4 GeV)

Laser pulse energy	[mJ]	0.35	1.0	2.0	3.0
max. modulation $\tilde{\delta}$ for eq.8	10^{-3}	4.51	7.22	10.0	12.2
triangle normalization $F_{\triangle}$ from eq.15		0.623	0.553	0.548	0.542
δ_{cut} for tracking	10^{-3}	3.0	3.0	3.5	3.5

The coordinates of the tracked particles at the location of the radiator[s] were written to files at every turn in order to do further processing using other IDL-programs: assuming that every electron in TRACY continues as a photon from the radiator centre, the particles were tracked further down the beamline to the FE-slits and finally to the BL-slits (see fig.6) by application of drift and toroid matrices. This neglects any diffraction effects, but includes the increase of effective emittance due to radiator dispersion. At FE and BL slits particles were filtered and the resulting intensity was normalized to the analytical formula by dividing the number of transmitted particles by $N_o \cdot F_{\triangle}$ since N_o particles make up the complete histogram from fig.4, where the triangular distribution was fitted to.

The figure beside shows as an example the halo in turn 1000 after modulation for SLS-FEMTO. The halo appears to be completely filamented. The empty center is due to the fact, that the core region was cut out. All grey particles are blocked by the FE-slits. The magenta, red, orange, yellow, green particles correspond to $1 \ldots 5$ sigma filtering at the BL-slits. The blue particles are beyond 5 sigma.

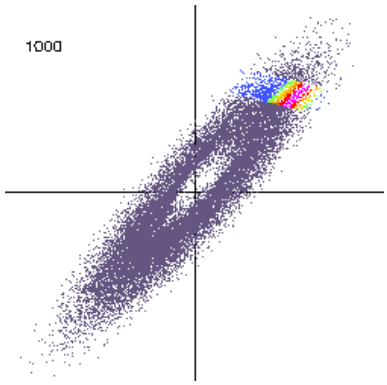

8 Results

Calculations were done for SLS-FEMTO, SOLEIL-CRISTAL and SOLEIL-TEMPO with parameters listed in appendix A. In addition or in deviation from these, following parameters were set:

		FEMTO	CRISTAL	TEMPO
Slicing rep. rate	[kHz]	1	10	
Max. modulation $\tilde{\delta}_p$	10^{-3} (MeV)	10.0 (24)	7.2 (20)	
FE slit positions	[mm]	16 ± 1.55	2.5 ± 0.5	3.5 ± 0.5
BL slit positions	[μm]	± 140	± 380	± 48
Toroid tangential radius	[m]	5541	137	135

Using our model, the situation was optimized with regard to signal intensity and signal to halo ratio using the FE-slit inner blade as the main parameter, however the width of the FE-slit was kept constant – in case of FEMTO it is not available as a parameter anyway. The toroid tangential radii in all cases have been optimized for optimum halo suppression and result in focusing the beam to the BL-slits, which were set to $\pm 2\sigma$ of the beam width.

For FEMTO the toroid translation and acceptance from eq.44 is given as FE slit position in the table above. For CRISTAL the toroid radius value is sligthly beyond the maximum of 121 m listed in the appendix. Using this maximum value would result in a 20% higher halo background. The middle of 3 available BL-slits has been used. For the other two, the optimum radius is even further out of the operating range.

The best toroid radius value found for TEMPO agrees with the value for an ideal point-to-point imaging, see eq.27. The value given in the appendix is wrong probably.

The results are shown in figs. 7, 8 for FEMTO, figs. 9, 10 for CRISTAL and figs. 11, 12 for TEMPO:

8.1 Normalized phase space

The normalized phase space (χ, χ') is plotted at the location of the radiator midpoint as shown above schematically in figs.3, 5 and 6. For FEMTO with no dispersion in the radiator, all halo-circles are concentric.

The initial modulation is shown as red line, the maximum halo as blue circle. 1σ and 5σ contours of the core beam are shown as black solid, resp. dashed circles. The FE and BL slits are shown as blue and cyan corridors. Inside the yellow rhomboid of intersection the accepted signal is shown as thick red line, and the accepted halo as blue arcs. The red dotted crosshair marks the coordinate offset when moving from the radiator/FE system to the BL system. Following slicing efficiencies were obtained for the parameters mentioned above:

			FEMTO	CRISTAL	TEMPO
Slicing efficiency	eq.17	10^{-4}	0.87	2.8	2.0
Total efficiency	eq.18	10^{-9}	0.8	66	48

The impressive factor 100 advantage of the SOLEIL proposals to the present SLS-FEMTO is due to higher rep rate (factor 10), larger sliced bunch current (factor 2.5), shorter bunches (factor 1.6) and wider FE-acceptance (factor $2-3$) – as previously mentioned, FEMTO is restricted by the limited horizontal acceptance of the grazing incident toroidal mirror.

8.2 Halo decay curve

Halo intensities accepted by the FE slits and by FE & BL slits as functions of time are shown as blue, resp. red lines. The accepted signals are the symbols at $t = 0$. Intensities are normalized to the triangular fit from fig.4, resp. to the distribution function from eq.8. Since there is no dispersion in the radiator of SLS-FEMTO, the halo decays smoothly, whereas the dispersive radiators of SOLEIL lead to a modulation with the synchrotron oscillation. For the given laser repetition rate, the halo decay curve is sampled according to eq.32 and gives the following results for the ratio of halo to signal:

	FEMTO	CRISTAL	TEMPO
Halo to signal ratio $H^{\mathrm{BL}}/S^{\mathrm{BL}}$	0.06	0.21	0.29

Considering that the rep rate is 10 times higher for SOLEIL, the halo suppression is still better by a factor 2–3 thanks to the synchrotron oscillation. At SLS-FEMTO the measured halo to signal ratio at 1 kHz rep. rate was 7%, which agress well with the model.

8.3 Comparison of model and tracking

Intensity as a function of turn number is shown in dark blue for FE acceptance, and in light blue for FE & BL transmission. The insert is a magnification for the first few turns. The signal is the intensity in turn 0. The model is shown as purple (FE), resp. red (FE & BL) lines, resp. crosses.

It is interesting to note that due to high chromaticity ($+5$) and larger modulation amplitude the halo filaments rather fast in case of SLS, where for SOLEIL with lower chromaticity (≈ 0) the betatron oscillation is visible much longer.

The model reproduced quite well the shape of the halo decay curve and the relative intensities, however in absolute values the model generally provides about $20-50\%$ larger numbers than tracking, which is not yet understood[5]. Therefore the data were normalized to the FE signal S^{FE} for overplotting.

[5] probably bad statistics in tracking: only a few 100 particles contribute to signal and halo

The table below compares model and tracking data of the absolute values of the signals and the total integrals over the halo decay curves (i.e. the halo intensity if the laser repetition rate would equal the revolution frequency).

		FEMTO	CRISTAL	TEMPO
S^{FE}	model / **tracking**	0.032 / **0.027**	0.062 / **0.054**	0.045 / **0.042**
S^{BL}		0.030 / **0.024**	0.059 / **0.047**	0.043 / **0.040**
$\sum H_i^{\mathrm{FE}}$		12 / **9.7**	28 / **21**	2.6 / **1.7**
$\sum H_i^{\mathrm{BL}}$		2.1 / **1.5**	1.3 / **1.0**	1.2 / **1.0**

Considering the approximations and simplifications of the model, the agreement with tracking is acceptable and supports confidence in the model.

8.4 Signal and halo vs. FE slit position

Red and blue symbols mark FE, resp. FE & BL signal, solid lines the integrated halo and dashed lines the core beam intensity.

Best halo suppression is achieved if the FE & BL acceptance rhomboid is moved near the peak of the modulation, because then the halo disappears most fast from the acceptance. This also provides the shortest X-ray pulses. However, the signal intensity is low and can be increased on expense of pulse length and halo noise by moving the rhomboid closer to the centre by shifting the FE-slits to the inside. In reality, the best working point will be found empirically.

8.5 Halo vs. slicing repetition rate

Blue and red lines show the total halo accepted by the FE, resp. FE & BL slits as a function of the laser repetition rate. The signal intensity is indicated by horizontal blue and red lines, the core background by cyan lines. The black lines correspond to a linear fit for halo intensity as a function of rep. rate, from which characteristic values of rep. rate are calculated and shown in the table below: the maximum rep.rate where the halo has disappeared due to damping from the acceptance before the next laser shot, and the rep. rate where halo and signal are of same intensity:

		FEMTO	CRISTAL	TEMPO
Rep. rate for $H^{\mathrm{BL}}/S^{\mathrm{BL}} = 0$	[kHz]	0.40	0.66	0.75
Rep. rate for $H^{\mathrm{BL}}/S^{\mathrm{BL}} = 1$	[kHz]	10.1	42.2	31.4

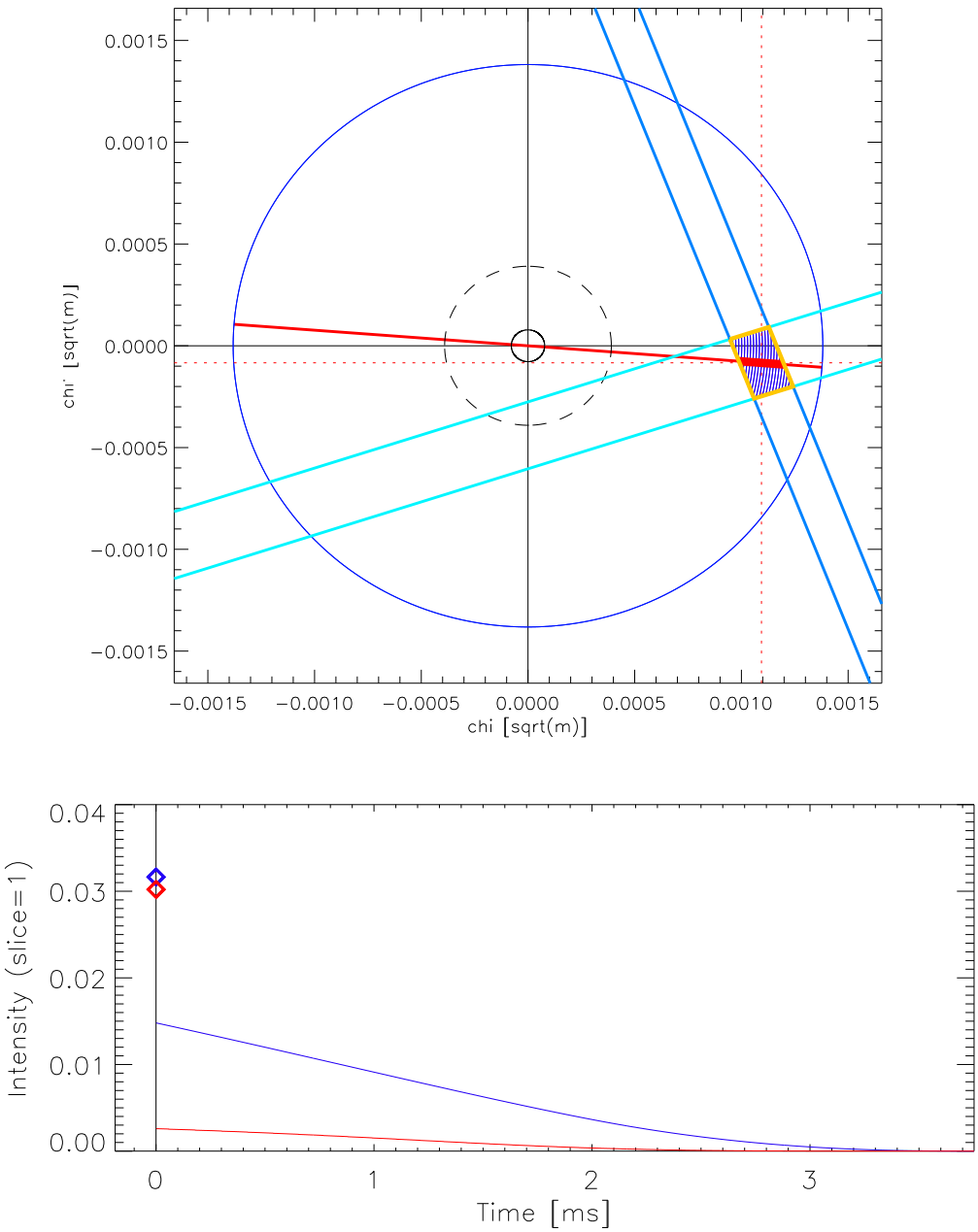

Figure 7: FEMTO: normalized phase space and halo decay

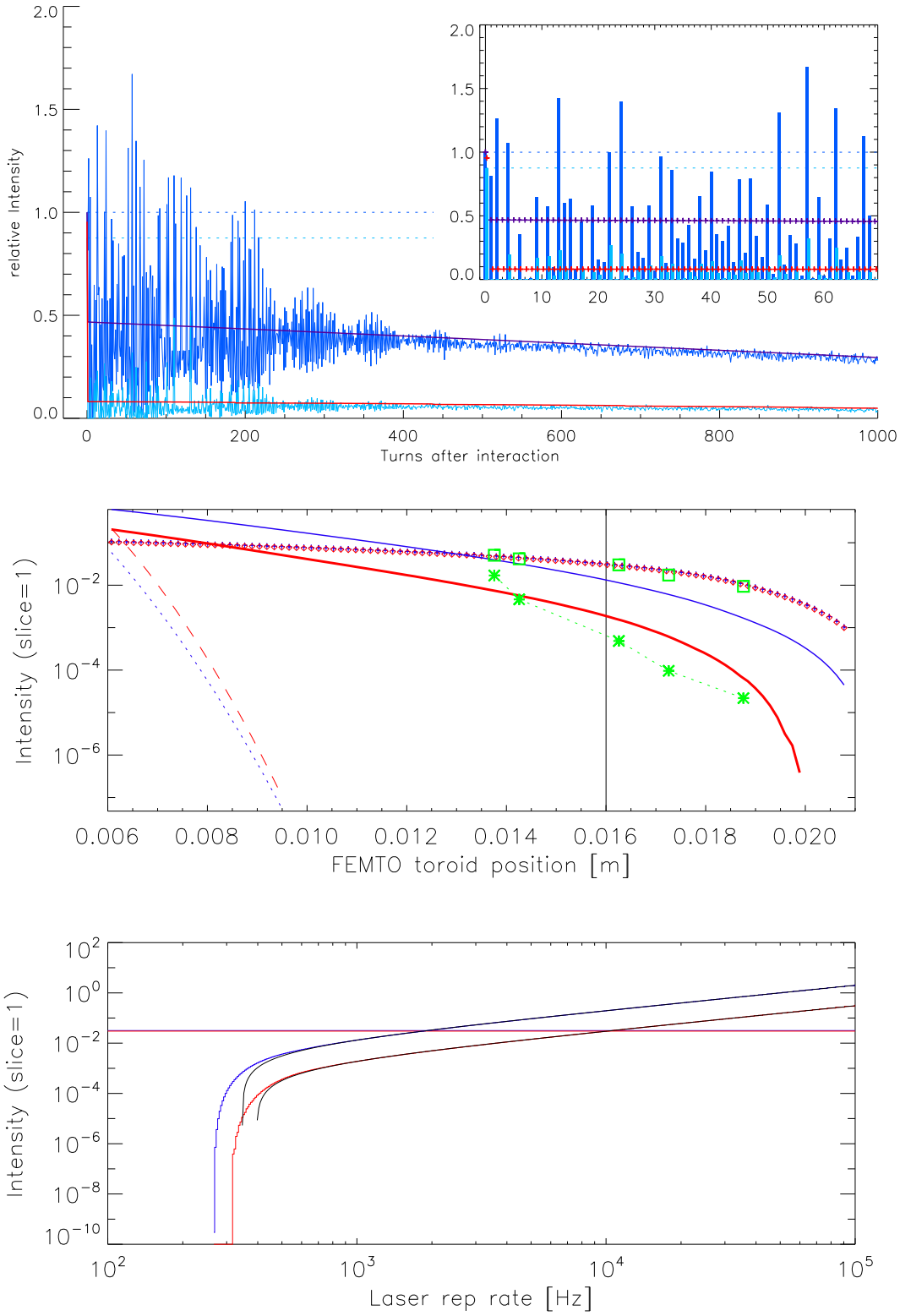

Figure 8: FEMTO: model vs. tracking, aperture and frequency scan

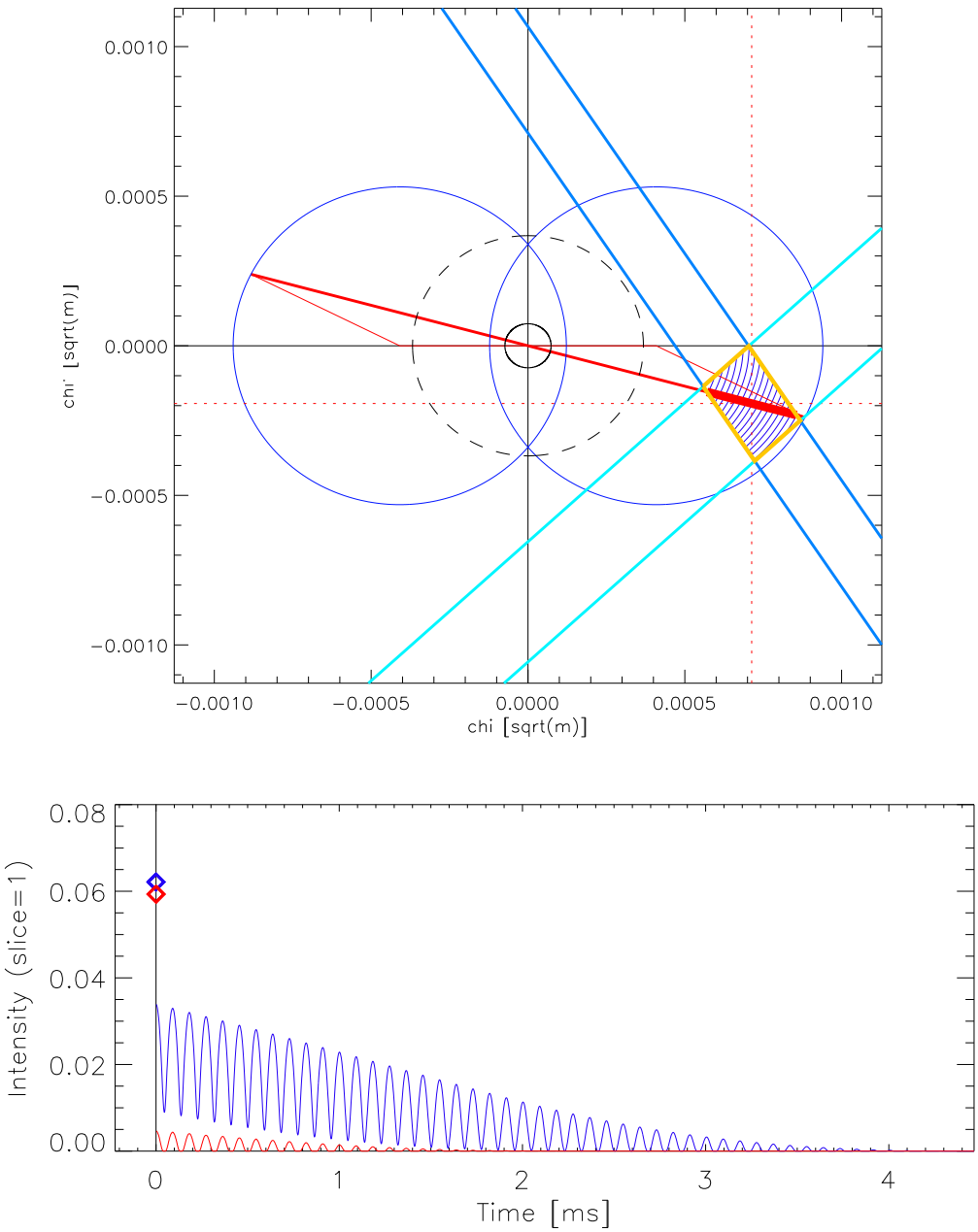

Figure 9: CRISTAL: normalized phase space and halo decay

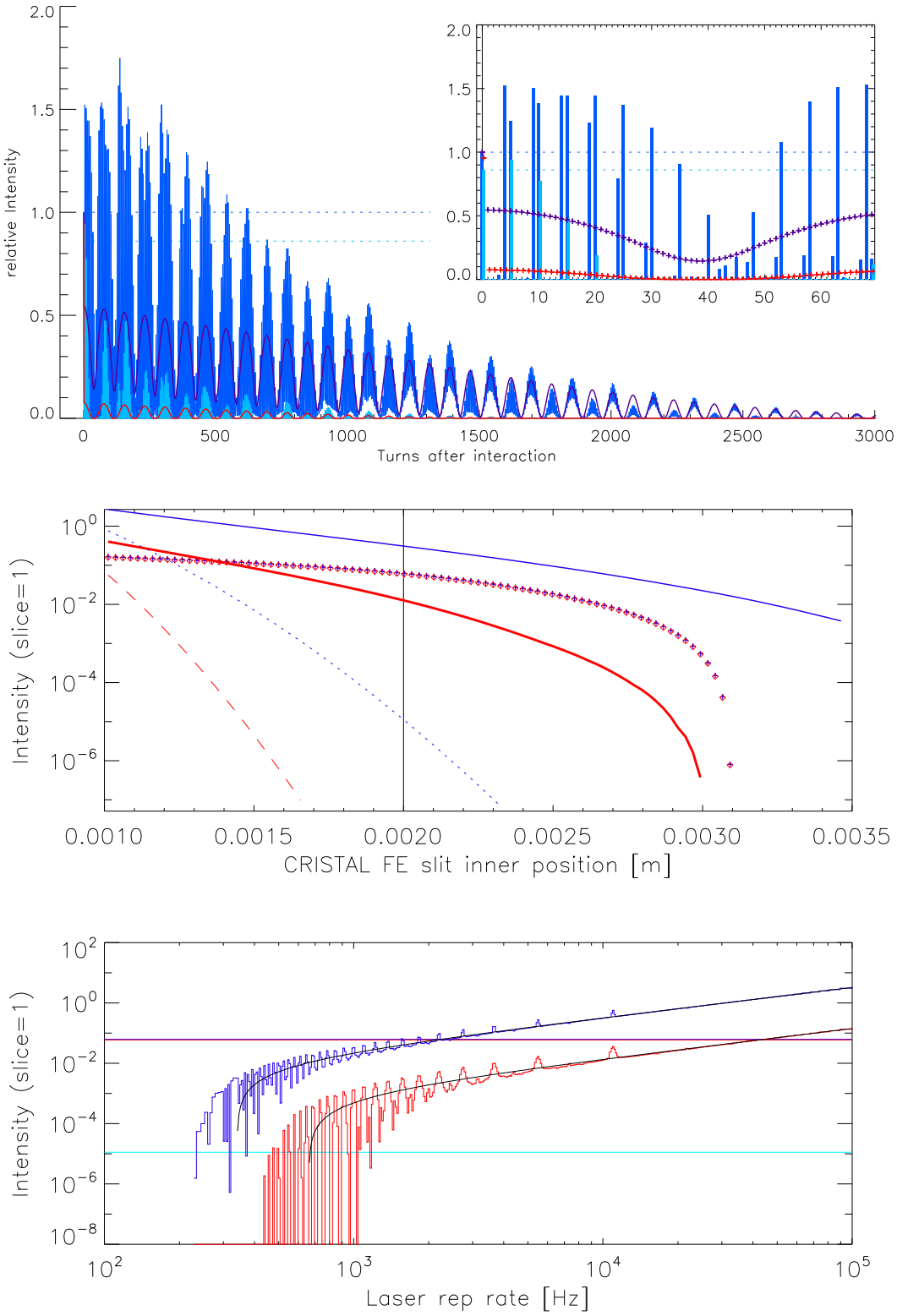

Figure 10: CRISTAL: model vs. tracking, aperture and frequency scan

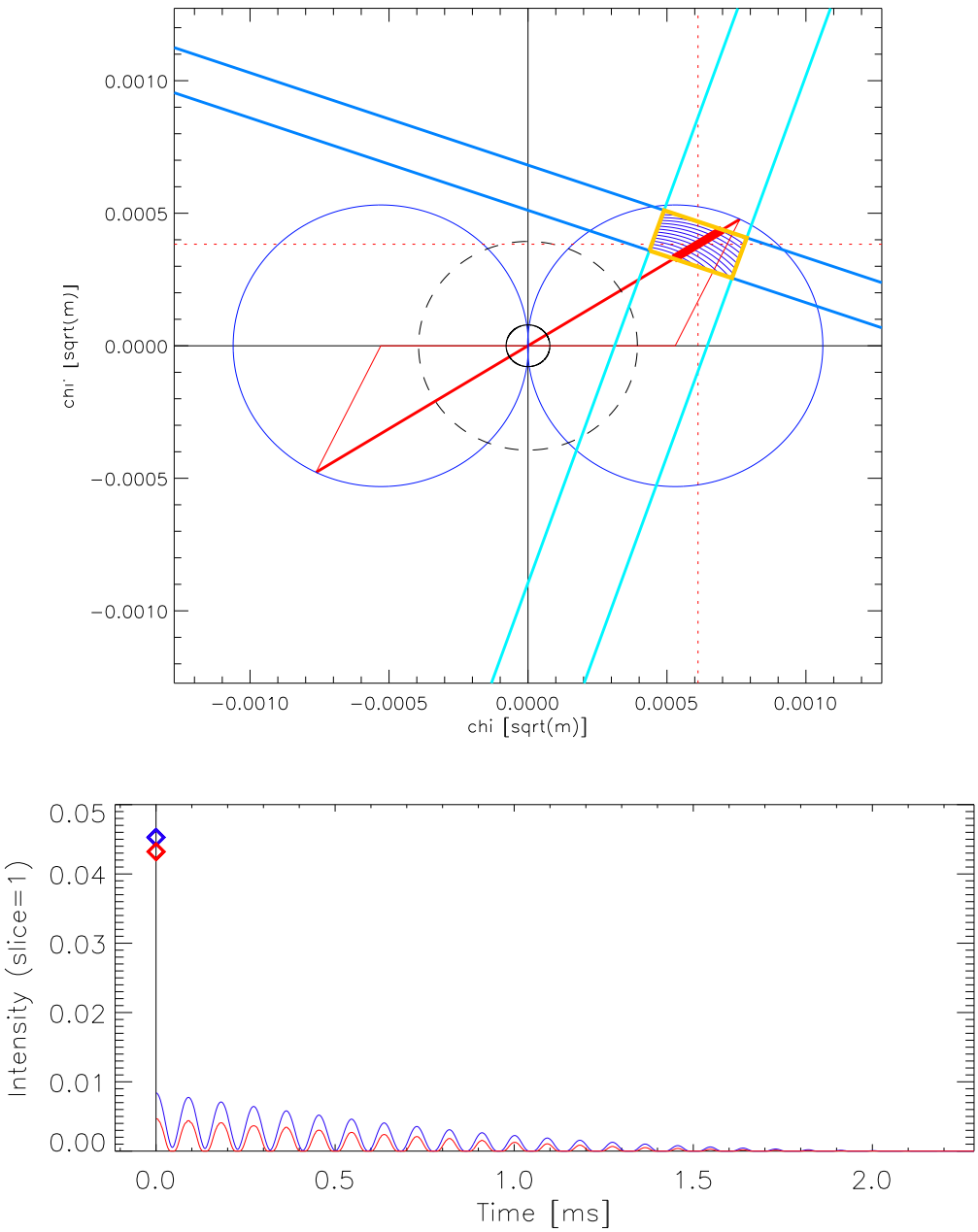

Figure 11: TEMPO: normalized phase space and halo decay

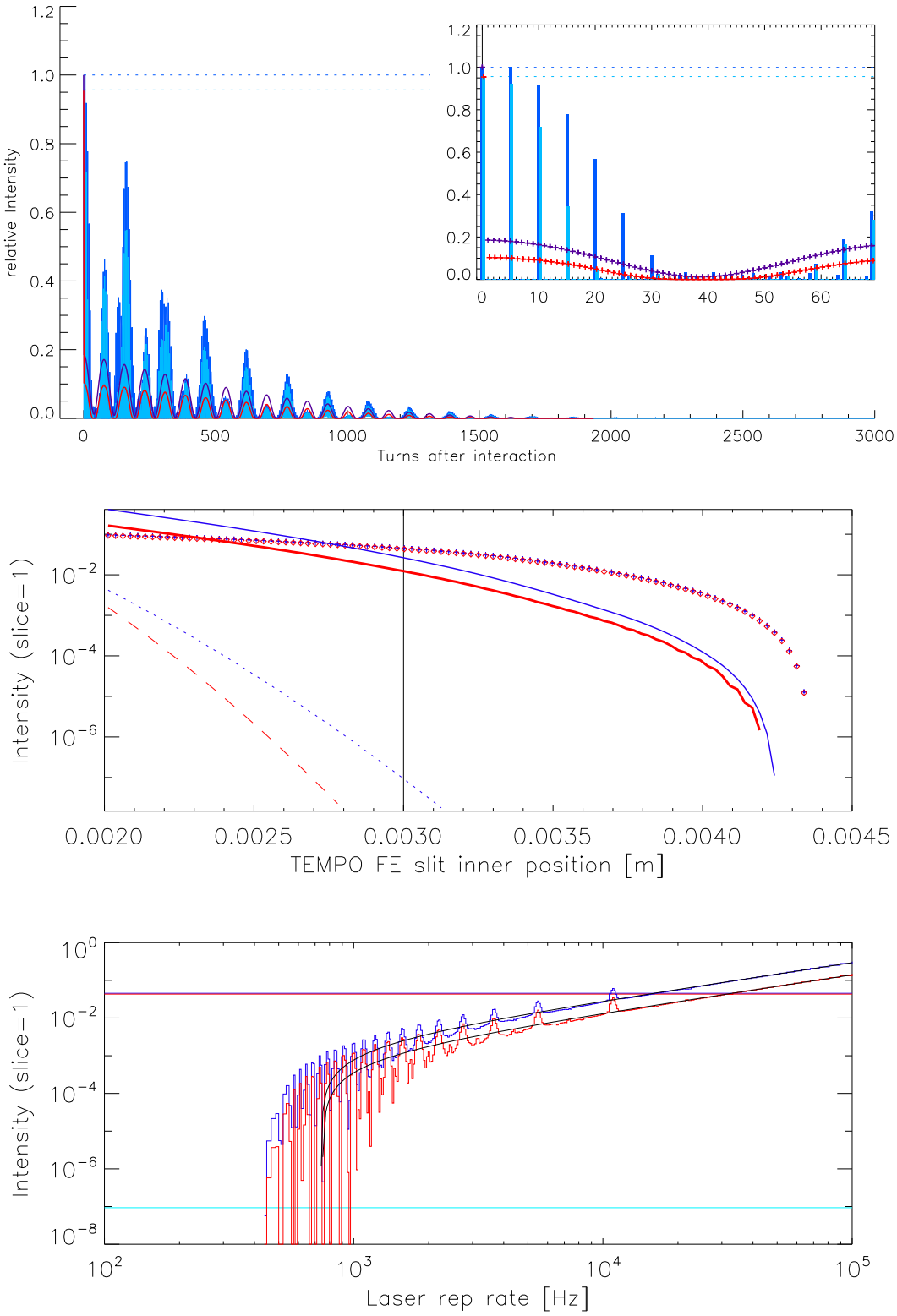

Figure 12: TEMPO: model vs. tracking, aperture and frequency scan

9 Discussion of results

9.1 Optimization strategy

Based on the optimizations using the model, the following strategy became clear to increase the signal and suppress the halo:

- Peak modulation is determined by the core beam background. Here, we considered only background from the core beam in the radiator, but the background from adjacent bending magnets may be much higher.
- The FE-slit positions are the most important parameter: moving them both out, i.e. towards the peak of the modulation reduces the signal, but even stronger the halo and strongest the core, and besides gives the shortest X-ray pulses. As a first guess one may set the inner blade to at least 5σ effective (incl. dispersion and diffraction) rms core beam width, and the outer blade to the peak of the modulation.
- The BL-slits have to be at the focus of the beam, which requires a tunable focusing element (toroid) in the beam line, and may be opened to about 2σ of the effective rms modulated beam width.
- Dispersion in the radiator undulator helps in halo suppression since the halo disappears temporarily from the acceptance due to synchrotron oscillations.
- A period-P filling pattern with P bunches sliced alternatingely gives a factor $\geq P$ better signal to halo ratio.

9.2 Comparison to measurements at SLS-FEMTO

The total slicing efficiency from eq.18 and listed in sec.8.1 gives the ratio of sliced photon flux to normal photon flux. The μXAS/FEMTO beamline operates at 6 keV and a relative bandwidth of $1.6 \cdot 10^{-4}$ set by the monochromators. At 400 mA beam current, the measured flux amounts to $7.5 \cdot 10^{12}$ ph/s/0.016% BW. The single bunch used for slicing has a current of 4 mA compared to 1 mA of a bunch in the normal train, which was already taken into account when calculating the total slicing efficiency. Furthermore a CVD filter taking 50% of intensity used in normal operation is removed for slicing. So another factor $F_{\mathrm{CVD}} = 2$ has to be applied, giving a flux of about $1.3 \cdot 10^4$ ph/s/0.016% BW at 6 keV and 1 kHz rep. rate, resp. about 80 photons per shot normalized to 0.1% BW for comparison with fig.13 showing a measurement of signal, halo and core photon counts as a function of FE-slit, i.e. toroid position. Signal and halo data have been added to fig.7 (green squares and stars) after division by $\mathrm{SE}_{\mathrm{total}} F_{\mathrm{CVD}} / S^{\mathrm{BL}}$ for normalization to the model (red diamonds resp. line in fig.7).

Note: since the abscissa of the measurement is only a relative coordinate, the measured signal photon numbers were looked up in the model curve to find the related toroid positions,

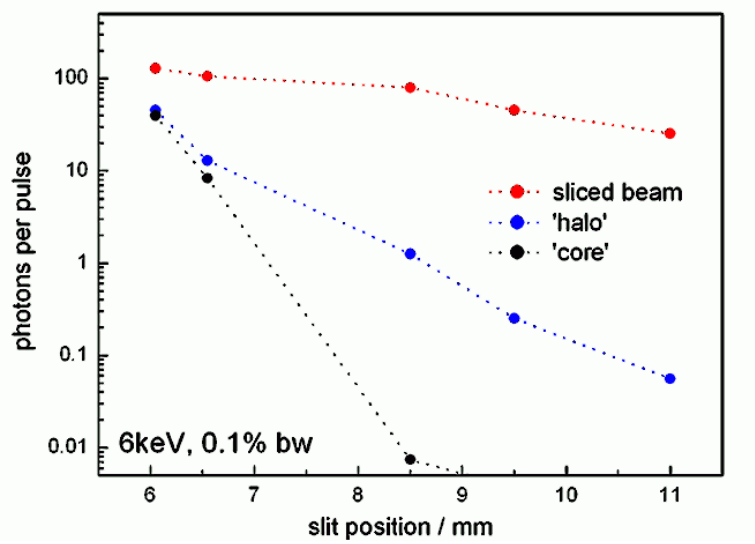

Figure 13: Measurement of signal, halo and core intensity as a function of front end slit position at SLS-FEMTO [4]

then the series of looked up positions was shifted relative to the series of measured positions by adjusting both mean values. Of course, any deviation from the counted signal photons from the model prediction would shift the points again, so any conclusion on agreement has to be taken with some care.

9.3 Alternative filling patterns at SLS

If the halo intensity is too high, there is still the possibility to have several bunches in the ring and to slice them alternatingely. Then the halo decay sampling rate is equal to the laser repetition rate divided by the number of bunches. The gating of the detectors is sufficiently fast (≈ 20 ns) to allow reasonable distances between the sliced bunches.

The number of bunches has to be odd, because in pumb-probe experiments only every second laser shot goes to the sample (pump) but every shot is used for slicing to create the X-ray pulse for analysis (probe) in order to have optimum background subtraction. An even number of bunches would introduce a systematic error, since different sets of bunches would be used for probing and for background determination.

In the SLS storage ring, due to beam loading effects, the filling pattern introduces a phase modulation, which is welcome basically, because it provides the Landau damping of coupled bunch instabilities by means of the 3^{rd} harmonic cavity, but it implies a temporal shift of bunch centres by about $0.4 \ldots 0.7$ ps/bucket (depending on cavity tuning) at 400 mA. In order to have a constant repetition time T_L when alternating between several bunches (instead of a $T_{L1}, T_{L2} \ldots$ series, which would be difficult to handle), the filling pattern needs a periodicity equal to the number of bunches to be sliced.

SLS has 480 buckets and is usually operated with a train of 390 bunches filled to about 1 mA plus a single bunch of about 4 mA current 30 ns in front of the train. The remaining gap (150 ns) is used for ion clearing and in order to introduce the phase modulation for Landau damping. A feedback procedure based on individual bunches current measurements controls the filling pattern [7]. At bunch charges higher than 4 mA coherent synchrotron radiation leads to a high background of THz radiation, which spoils the THz based diagnostics of the laser-beam overlap.

Alternative patterns using 3 or 5 evenly spaced bunches and shorter trains between have been investigated but found less stable due to reduced Landau damping. Eventually stability could be achieved by increasing the gaps, however this requires distribution of the 400 mA beam current on a smaller number of bunches and thus leads to reduced Touschek lifetime [1].

9.4 Comment on proposed laser slicing at SOLEIL

At 10 kHz slicing repetition rate and 10 mA single bunch current, both CRISTAL and TEMPO beam lines at SOLEIL can achieve a total slicing efficiency of about $5 \cdot 10^{-8}$ at a halo background level of about 25%. A break-even of halo and signal is reached for a rep. rate of $30 \ldots 40$ kHz. Diffraction effects were not yet included.

Dispersion in the radiators turns out to be an advantage for SOLEIL since halo suppression is supported well by the synchrotron oscillation. This advantage overcompensates the disadvantage of increased effective emittance due to dispersion. However, due to interference of the laser shots with the synchrotron oscillation exist some inconvenient combinations, which lead to a much higher halo background. But these cases could be easily avoided by a small change of synchrotron tune.

On the other hand, considering a dedicated slicing operating mode with 50 bunches of 10 mA (if feasible) a very high slicing rep rate of 50–100 kHz (if feasible) would result in 1–2 kHz rep. rate per bunch, and then the interference of rep.rate and synchrotron oscillation (see the frequency scans in figs.10, 12) could even be exploited to find combinations for lowest halo.

9.5 Comment on proposed upgrade of SLS-FEMTO

The FE-slit acceptance limitation could be widened relatively by reducing the laser modulation, than the whole phase space diagram from fig.7 is demagnified, but not the FE corridor. But the gain is signal (factor 2) is accompanied by an even higher increase of the halo. Moving out the FE-slit to reduce both signal and halo returns to the present performance, so reducing the modulation gains nothing.

Introducing dispersion in the radiator would reduce the halo in the way as observed in the SOLEIL studies. Modification of optics while keeping all contraints on phase advances however is difficult. Very preliminary studies however indicate a 50% improvement.

In the present configuration, the only way to increase the flux while keeping the same signal to noise level is using the period-5 filling pattern and upgrade the laser from 2 to 10 kHz.

10 Conclusion

A model has been established and calibrated, which allows visualization and fast interactive optimization of the parameters in a laser slicing setup.

The performance of proposed laser slicing at CRISTAL and TEMPO beam lines of SOLEIL was investigated and lead to about $5{\cdot}10^{-8}$ total slicing efficiency (compared to normal operation at 500 mA) and about 25% signal to halo ratio for 10 kHz slicing rate and 10 mA bunch current. Considering alternate slicing of many bunches, even a laser repetition rate of up to 100 kHz may be feasible.

The performance of the existing laser slicing at the FEMTO beam line of SLS was modelled and compared with real data. A slicing efficiency of $8{\cdot}10^{-10}$ and 6% signal to halo ratio was found for 1 kHz laser repetition rate and 4 mA bunch current. Measurements of flux and signal to halo ratio agree well with the model.

A SLS and SOLEIL parameter tables

A.1 SLS and SOLEIL storage ring parameters

			SLS	SOLEIL [10]
Energy	E	[GeV]	2.411	2.75
Revolution time	T_o	μs	0.96	1.18
Working point	ν_x / ν_y		20.43 / 8.74	18.20 / 10.31
Emittance	ϵ	[nm rad]	6.1	4.1
Rel. energy spread	σ_δ	10^{-3}	0.86	1.02
Horizontal damping time	τ_x	[ms]	8.0	6.5
Longitudinal damping time	τ_s	[ms]	4.0	3.25
RF voltage	V_{RF}	[MV]	2.2	4.0
Synchrotron tune	ν_s		0.0062	0.0065
rms bunch length$/c$	σ_t	[ps]	16	10
Total beam current	I_o	[mA]	400	500
Number of bunches	B		390	416
Sliced bunch current	I_s	[mA]	4	10
Beam parameters at modulator centre				
Beta function	β_m	[m]	9.265	4.175
Alpha function	α_m		0.68	≈ 0
Dispersion	η_m	[m]	-0.0617	0.15
Dispersion slope	β'_m		-0.0413	≈ 0

SLS data for synchrotron tune and bunch length are without 3rd harmonic cavity.

A.2 SLS μXAS/FEMTO beamline parameters

Point of reference	radiator U19 centre
Beta function	8.7 m
Alpha function	-2.07
Stored beam dispersion	0 m
Stored beam dispersion slope	0
Modulated dispersion	0.4153 m
Modulated dispersion slope	0.0952
Phase advance mod→rad	86°
Toroid at	17.315 m
Horizontal beam line slits at	31.865 m
Toroid orientation	horizontal
Toroid incident angle	3.1 mrad (var.)
Toroid tangential radius	$5.4 \ldots \infty$ km
Toroid sagittal radius	0.1075 m
Toroid length	1.0 m

A.3 SOLEIL CRISTAL beamline parameters[11]

Point of reference	radiator HU20 centre
Beta function	18.19 m
Alpha function	≈ 0
Stored beam dispersion	0.2416 m
Stored beam dispersion slope	≈ 0
Modulated dispersion	0.5217 m
Modulated dispersion slope	-0.008
Phase advance mod→rad	210°
Front end slits at	12 m
Toroid at	19 m
Horizontal beam line slits at	5, **15**, 16.5 m
Toroid orientation	horizontal
Toroid incident angle	9.48° (for 12 keV)
Toroid tangential radius	91…121 m
Toroid length	0.1 m

A.4 SOLEIL TEMPO beamline parameters[12]

Point of reference	centre of medium straight
Beta function	4.18 m
Alpha function	≈ 0
Stored beam dispersion	0.150 m
Stored beam dispersion slope	≈ 0
Modulated dispersion	0.216 m
Modulated dispersion slope	0.03
Phase advance mod→rad	839°
Radiator HU80 centre at	-0.416 m
Radiator HU44 centre at	1.332 m
Front end slits at	12 m
Toroid at	20.945 m
Horizontal beam line slits at	23.538 m
Toroid orientation	horizontal
Toroid incident angle	2°
Toroid tangential radius	367 m [?]
Toroid sagittal radius	0.163 m
Toroid length	0.12 m

B Imaging properties of a toroidal mirror

A toroidal mirror is a surface shaped as the section of a torus as shown in fig. 14; it focuses in both transverse planes. For use in an X-ray beam line, one of the incident angles (here: the horizontal angle α) has to rather small to provide sufficient reflectivity. The toroid shown in the figure is located at the origin of the coordinate system, with radii of curvature R in the horizontal, called tangential radius, and Q in the vertical, called sagittal radius. A vector $\vec{t}$ of the toroid surface thus is given by

$$\vec{t} = \begin{pmatrix} R & -(R-Q)\cos\phi & -Q\cos\phi\cos\theta \\ & & Q\sin\theta \\ & (R-Q)\sin\phi & +Q\sin\phi\cos\theta \end{pmatrix} \tag{33}$$

The normal vector of the tangential plane in a point of the toroidal surface is given by

$$\vec{n} = \begin{pmatrix} -\cos\phi\cos\theta \\ \sin\theta \\ \sin\phi\cos\theta \end{pmatrix} \tag{34}$$

The angles ϕ and θ will be very small. Keeping up to second orders approximates the toroid by a paraboloid:

$$\vec{t} \approx \begin{pmatrix} R\phi^2/2 & + & Q\theta^2/2 \\ & Q\theta & \\ R\phi & & \end{pmatrix} \qquad \vec{n} \approx \begin{pmatrix} -1+\phi^2/2+\theta^2/2 \\ \theta \\ \phi \end{pmatrix} \tag{35}$$

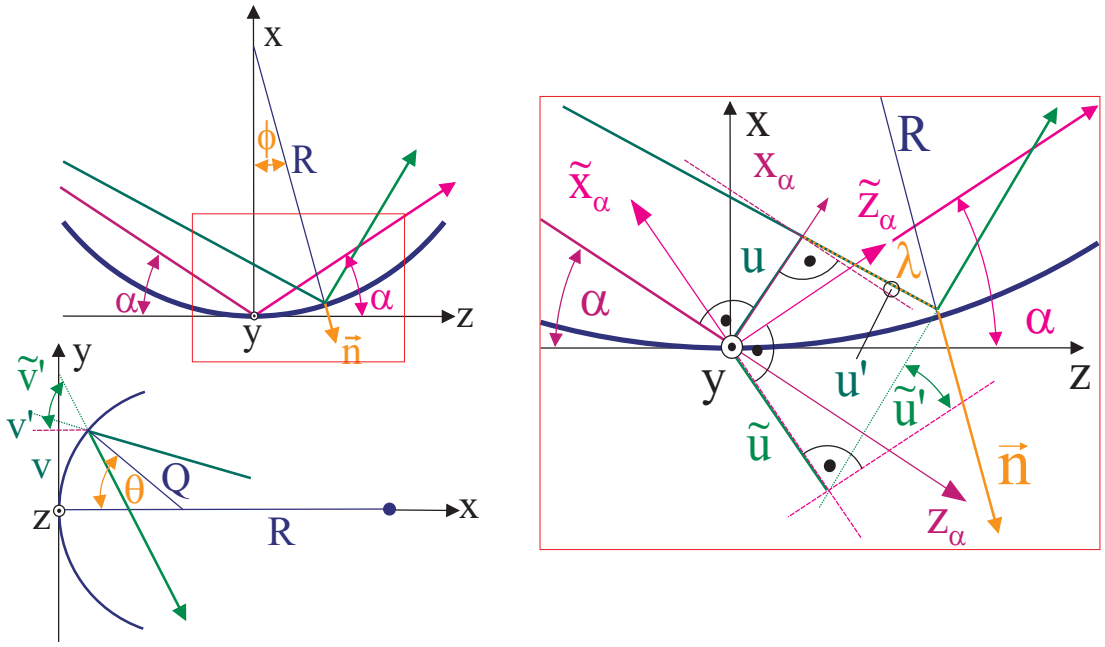

Figure 14: Toroidal mirror: right figure is a magnifaction of top left figure's centre.

An incoming photon ray is characterized by horizontal and vertical offsets u, v and divergences u', v' defined in the coordinate system of the centre ray, which is rotated by the incident angle α. So a rotation by α gives a point on the incoming ray $\vec{a}$ in the toroid system in first orders of u, v, u', v':

$$\vec{a} = \begin{pmatrix} \cos\alpha & 0 & -\sin\alpha \\ 0 & 1 & 0 \\ \sin\alpha & 0 & \cos\alpha \end{pmatrix} \cdot \left[\begin{pmatrix} u \\ v \\ 0 \end{pmatrix} + \lambda \begin{pmatrix} u' \\ v' \\ 1 \end{pmatrix} \right] \qquad \lambda \in \boldsymbol{R} \tag{36}$$

The point $\vec{r}$ where the ray hits the toroid is calculated from $\vec{t} = \vec{a}$ and solving for λ, ϕ, θ. Eq.34 then provides the normal vector. The solutions in first order are

$$\vec{r} = \begin{pmatrix} 0 \\ v \\ u/s \end{pmatrix} \qquad \vec{n} = \begin{pmatrix} -1 \\ v/Q \\ u/(Rs) \end{pmatrix} \qquad \text{with} \quad \begin{matrix} c = \cos\alpha \\ s = \sin\alpha \end{matrix} \tag{37}$$

The direction unit vector $\vec{k}$ of the incident ray is given by the last term in eq.36. Indices $\parallel$ and $\perp$ define its components parallel and orthogonal to the normal, and $\tilde{\vec{k}}$ the outgoing unit vector. Reflection then is described by

$$\tilde{\vec{k}}_\parallel = -\vec{k}_\parallel, \quad \tilde{\vec{k}}_\perp = \vec{k}_\perp \quad \longrightarrow \quad \tilde{\vec{k}} = \vec{k} - 2(\vec{k} \cdot \vec{n})\, \vec{n} \tag{38}$$

We get for the outgoing ray unit direction in first order

$$\vec{k} = \begin{pmatrix} cu' - s \\ v' \\ su' + c \end{pmatrix} \qquad \longrightarrow \qquad \tilde{\vec{k}} = \begin{pmatrix} s - cu' + \frac{2c}{Rs}u \\ v' - \frac{2s}{Q}v \\ c + su' - \frac{2}{R}u \end{pmatrix} \tag{39}$$

A point of the reflected vector is given by $\tilde{\vec{a}} = \vec{r} + \tilde{\lambda}\tilde{\vec{k}}$ in the toroid coordinate system. The outgoing system is rotated by the angle $-\alpha$, so another rotation α has to applied, giving

$$\tilde{\vec{a}}_\alpha = \begin{pmatrix} -u \\ v \\ \frac{c}{s}u \end{pmatrix} + \tilde{\lambda} \cdot \begin{pmatrix} -u' + \frac{2}{Rs}u \\ v' - \frac{2s}{Q}v \\ 1 \end{pmatrix} \tag{40}$$

Finally, the offsets and angles in the outgoing system are defined in the plane at the toroid origin and orthogonal to the outgoing centre ray, i.e. we get them from solving for $\tilde{\lambda}$ setting $\tilde{a}_{\alpha,z} = 0$:

$$\tilde{u} = -u \quad \tilde{u}' = -u' + \frac{2}{Rs}u \quad \tilde{v} = v \quad \tilde{v}' = v' - \frac{2s}{Q}v \tag{41}$$

or, combined in 2×2 transfer matrices:

$$\tilde{\vec{u}} = \begin{pmatrix} -1 & 0 \\ \frac{2}{R\sin\alpha} & -1 \end{pmatrix} \vec{u} \qquad \tilde{\vec{v}} = \begin{pmatrix} 1 & 0 \\ -\frac{2\sin\alpha}{Q} & 1 \end{pmatrix} \vec{u} \tag{42}$$

So the toroid is focusing in both dimensions with focal lengths

$$f_x = \frac{R\sin\alpha}{2} \qquad f_y = \frac{Q}{2\sin\alpha} \tag{43}$$

It is also worth to note, that the horizontal acceptance of a toroid of length L (in z-direction) is limited by

$$|\lambda| = |u|\cot\alpha \leq \frac{L}{2} \quad \rightarrow \quad |u| \leq \frac{L\tan\alpha}{2}. \tag{44}$$

References

[1] N. Abreu et al., “New Filling Pattern for SLS-FEMTO”, Internal report SLS-TME-TA-2009-0317.

[2] H.-J. Bäcker et al., “Layout of a femto-second X-ray source at BESSY II”, Proc. PAC 2003, Portland, p.836.

[3] P. Beaud, PSI, priv. comm.

[4] P. Beaud, S. Johnson, “Status of the FEMTO project”, presentation at EPFL, Lausanne, Oct.25, 2006.

[5] M. Böge, “Update on TRACY-2 documentation”, Internal Report SLS-TME-TA-1999-0002.

[6] W. Joho, “The effective emittance of a photon source”, SLS-note 3/93

[7] B. Kalantari et al., “Bunch pattern control in top up mode at the SLS”, Proc. EPAC 2004, p.2885.

[8] D. Kalantaryan et al., “The acceptance and photon beam formation in SLS FEMTO”, Proc. EPAC 2008, Genova.

[9] μXAS beam line at SLS, `http://sls.web.psi.ch/view.php/beamlines/mxas/optics`

[10] A. Nadji et al., “Femto-second electron beam slicing project at SOLEIL”, Proc. EPA 2004, Lucerne, p.2332.

[11] S. Ravy, SOLEIL, priv. comm.

[12] F. Sirotti, SOLEIL, priv. comm.

[13] A. Streun, “The influence of the electron beam’s divergence on the photon beam’s emittance”, SLS-note 4/93.

[14] A. Streun, “SLS-FEMTO: beam halo formation and maximum repetition rate for laser slicing”, Internal Report SLS-TME-TA-2003-0222.

[15] A. Streun “Halo background in SLS-FEMTO”, Internal Report SLS-TME-TA-2003-0311.

[16] A.Streun et al., “Sub picosecond X-ray source FEMTO at SLS”, Proc. EPAC 2006, Edinburgh, p.3427.